Journal of Energy Chemistry 112 (2026) 1014–1025

Contents lists available at ScienceDirect

Journal of Energy Chemistry

journal homepage: www.elsevier.com/locate/jechem

http://www.journals.elsevier.com/journal-of-energy-chemistry/

Optimized selectivity in CO_2 electrochemical reduction using amorphous CuNi catalysts: insights from density functional theory and machine learning simulations

Akshayini Muthuperiyanayagam [a], Enrico Pedretti [b], Maria Clelia Righi [b,*], Devis Di Tommaso [a,c,*]

[a] Department of Chemistry, School of Physical and Chemical Sciences, Queen Mary University of London, London E1 4NS, United Kingdom
[b] Department of Physics and Astronomy "Augusto Righi", University of Bologna, Via Pichat 6/2, 40127 Bologna, Italy
[c] Digital Environment Research Institute, Queen Mary University of London, Empire House, London E1 1HH, United Kingdom

ARTICLE INFO

Article history:
Received 24 May 2025
Revised 8 August 2025
Accepted 23 August 2025
Available online 14 September 2025

Keywords:
Electrochemical CO_2 reduction
Amorphous alloys
Machine learning forcefield
Ethanol formation

ABSTRACT

Amorphous materials represent a promising platform for advancing CO_2 electrochemical reduction due to their inherently diverse coordination environments. In this study, we demonstrate computationally the superior performance of amorphous CuNi alloys for CO_2 electrochemical reduction. By integrating machine learning forcefields for efficient structure generation and density functional theory for subsequent structural refinement and property calculations, we reveal the potential of these disordered systems to outperform their crystalline counterparts. Machine learning forcefields can generate a bulk structure containing a mixture of Cu and Ni atoms, resulting in enhanced catalytic performance. Effective screening of the amorphous surfaces is used to identify undercoordinated Cu and Ni sites in the amorphous structure to synergistically promote selective CO production and favor ethanol formation over ethylene via the stabilization of the *COCHO intermediate, resulting in significantly lower Gibbs free energy changes compared to the crystalline counterpart. The varying atomic coordination environments on amorphous surfaces promote both C–C bond formation and subsequent proton-electron transfer, leading to ethanol formation. These findings demonstrate the superior catalytic performance of amorphous CuNi, highlighting its potential for efficient and selective electroreduction of CO_2.

1. Introduction

The conversion of carbon dioxide (CO_2) into valuable chemicals is a key strategy for carbon utilization. In CO_2 electrolysis, CO_2 is upgraded into small oxo-hydrocarbons ($C_xH_yO_z$) using water and electricity in an electrolyser, at room temperature and ambient pressure. When powered by renewable technologies or low-carbon electricity, CO_2 electrolysis has the potential for economic and environmental viability, contingent upon performance metrics [1]. The electrochemical CO_2 reduction reaction (CO_2RR) into various products ($CO_2 + n(H^+ + e^-) \rightarrow$ Product $+ mH_2O$) can produce a range of valuable oxo-hydrocarbons. These include one-carbon (C_1) compounds such as formic acid (HCOOH), carbon monoxide (CO), methane (CH_4) and methanol (CH_3OH), as well as multi-carbon (C_{2+}) products like ethylene (C_2H_4), ethanol (C_2H_5OH) [2,3]. For CO_2 electrolysis to impact on the gigaton (Gt) scale, the production of ethylene (140 Mt/yr) and ethanol (106 Mt/yr) represent attractive products, offering a combination of high product value and large carbon intensity [4].

Copper (Cu) has emerged as a widely used electrocatalyst due to its unique ability to convert CO_2 into a variety of oxo-hydrocarbons [5–8]. Although achieving sufficiently high faradaic efficiency (FE) is crucial for the economic viability of CO_2 electrolysis, the generation of C_{2+} products like ethanol with a FE of 80 % [9] or above remains a challenge [10]. Key limitations include high reaction overpotential [11], competition with hydrogen evolution reaction (HER, $H^+ + e^- \rightarrow \frac{1}{2}H_2$) [12], as well as complex reaction mechanism with various intermediate steps, making it difficult to understand and control the reaction pathway leading to poor product

* Corresponding authors at: Department of Chemistry, School of Physical and Chemical Sciences, Queen Mary University of London, London E1 4NS, United Kingdom (D.D. Tommaso); Department of Physics and Astronomy "Augusto Righi", University of Bologna, Via Pichat 6/2, 40127 Bologna, Italy (M.C. Righi).

E-mail addresses: clelia.righi@unibo.it (M.C. Righi), d.ditommaso@qmul.ac.uk (D.D. Tommaso).

https://doi.org/10.1016/j.jechem.2025.08.089
2095-4956/

selectivity [13–15]. Therefore, improving the selectivity of Cu for CO_2RR involves strategies such as surface morphology modification [16,17], nano structuring [18,19], and alloying [20–22]. In recent years, amorphous catalysts have emerged as a promising class of materials that can effectively leverage these factors to enhance electrocatalytic performance.

Amorphous materials are defined by their disordered atomic arrangement, lacking the long-range order and periodicity that characterize crystalline solids [23]. This results in a high density of dangling bonds and defects within the material [24]. These structural features can provide a greater number of actives sites, potentially leading to enhanced product selectivity [25]. Duan et al. were the first to report the synthesis and application of Cu amorphous nanoparticles for CO_2RR, showing higher activity towards formic acid and ethanol with a total FE of 59 % at −1.4 V vs RHE [26]. Inspired by this study, Xiong et al. synthesized bimetallic Cu-Bi amorphous catalyst exhibiting even higher efficiency and selectivity towards HCOOH formation, with a maximum FE of 94.7 % at −1.0 V vs RHE [27]. Chen et al. oxidized metallic Cu with supercritical CO_2 to synthesize copper nanoparticles with an amorphous shell, which exhibited high selectivity towards C_{2+} products with a total FE of 84 %. Specifically, the FE for C_{2+} oxygenates was 65.3 %, including ethanol (46.7 %), *n*-propanol (7.1 %), and acetate (11.5 %) [28]. Moreover, in situ surface-enhanced Raman scattering (SERS) measurements used to monitor the formation of reaction intermediates revealed that amorphous Cu exhibits a higher surface coverage of the *CO intermediate compared to its crystalline counterparts [28]. Since *CO is a key intermediate in the CO(H) coupling pathway, which is essential for the formation of C_{2+} oxygenates, enhanced *CO coverage can promote C–C coupling and improve selectivity toward ethanol and other multi-carbon products.

The common findings across these studies are that amorphous catalysts exhibit a higher electrochemical active area (ECSA), as determined through double-layer capacitance measurements, compared to their crystalline counterparts [26–28]. This enhanced ECSA is attributed to the amorphous nature of the catalyst. The disordered structure likely leads to a higher density of active catalytic sites, resulting in improved catalytic activity towards CO_2RR. Furthermore, Chen et al. used operando XAS to demonstrate that the amorphous catalyst exhibited a higher abundance of low-coordinated atoms compared to crystalline Cu, which was hypothesized to be more favorable for CO_2 adsorption and reduction [28]. This hypothesis is corroborated by our previous computational study on monometallic amorphous Cu catalysts for CO_2RR [29], which revealed a diverse range of Cu coordination environments. These sites exhibited varying adsorption and electrocatalytic reduction capabilities, with low-coordinated Cu sites predicted to be more reactive towards CO_2 reduction.

Computational investigations of amorphous catalysts for complex reactions such as CO_2RR are hindered by two key challenges: generation of the amorphous structure and identification of the active catalytic sites. Atomistic models of amorphous systems are generally done via the "melt-and-quench" ab initio molecular dynamics (MD) simulations, but the use of density functional theory (DFT) is computationally demanding due to the long timescales required to accurately model the complex atomic rearrangements during the liquid to amorphous transition [30,31]. Characterizing the catalytic activity of amorphous surfaces is a challenge due to their structural characteristics. The diverse range of coordination environments presented by these materials requires a systematic investigation of multiple sites to identify those exhibiting optimal catalytic performance. To overcome these limitations, this study adopts an approach that combines machine learning forcefields (MLFFs) for rapid and efficient structure generation and DFT for subsequent structural refinement and property calculations.

MLFFs have recently emerged as a powerful tool to efficiently model complex materials by enabling large-scale molecular dynamics simulations at near-DFT accuracy [32]. While their application in electrocatalysis, especially CO_2 reduction, remains relatively limited [29], MLFFs are showing significant promise for modelling disordered catalyst surfaces and capturing coordination environments that are difficult to access by means of ab initio molecular dynamics [33]. This work MLFFs were used to generate realistic amorphous CuNi surfaces.

In this study, we present a computational investigation of an amorphous bimetallic CuNi alloy with a 1:1 ratio as a catalyst for CO_2RR, leveraging the known synergistic effects between Ni and Cu in alloy systems. Ni enhances electron transfer and stabilizes intermediates, while Cu facilitates C–C coupling, an essential step for forming multi-carbon products [34]. Experimentally, Romanovski et al. synthesised CuNi nanoparticles (12–18 nm) via solution combustion synthesis with varying Cu:Ni ratios (2:1, 1:1, and 1:2) [35]. Their MD simulations revealed a uniform atomic distribution and stable crystallization for the 1:1 ratio leading to homogenous bimetallic structure [35]. Wang et al. reported the excellent CO_2 reduction performance for CuNi clusters on N-doped porous carbon with stable performance for 30 h with a high CO FE of 95.1 % vs. RHE [20]. Li et al. further highlighted the impact of CuNi catalyst structure, demonstrating superior performance (CO FE of 94.0 % at −0.87 V vs RHE) for a phase separated CuNi/NC catalyst compared to an alloy CuNi/NC structure, emphasizing the importance of structural design in optimizing catalytic activity [36]. Therefore, CuNi system is used as a model system to develop the necessary computational methods to study the CO_2RR of bimetallic amorphous systems. Following the construction of the system, the Xsorb software [37,38] is used to systematically screen the amorphous catalyst surface, identifying potential active sites for CO_2 adsorption. The focus of the study will be on predicting the selectivity towards both C_1 (CO and HCOOH) and the C_2 (C_2H_5OH and C_2H_2) products. The CO_2 conversion to ethanol and ethylene is highly attractive due to their versatility in the chemical and energy industries as they can be used as feedstocks in the production of other chemicals or as feedstock for fuel cells [39–41]. Achieving higher FE for C_2 products enhances CO_2 conversion efficiency, reduces undesired by-products, and makes CO_2RR more economically competitive. While surface roughness and undercoordinated Cu sites are known to aid C_2 formation, the exact influence of Cu coordination environments on reaction pathways remains unclear [42,43].

2. Computational details

2.1. Computational workflow

The workflow in Fig. 1 outlines the computational approach utilized in this study. The MLFF generated using the Vienna Ab initio Simulation Package (VASP, version 6.4.2) [44,45], is employed to develop an atomistic model of the amorphous CuNi catalyst. The most stable adsorption sites are identified using the Xsorb software. Subsequently, free energy calculations are conducted at the DFT level to ascertain the free energy of reactions for the proton-coupled electron transfer (PCET) and C–C coupling steps involved in the electrochemical conversion of CO_2 into C_1 products (CO and HCOOH) and C_2 products (C_2H_5OH and C_2H_4). These calculations accounted for zero-point energy, entropy contributions, and solvent-dependent reaction pathways. The system considered in this study employed a 1:1 Cu:Ni ratio to ensure a balanced composition. This specific ratio also served to simplify the catalytic model, enabling us to focus on developing the proposed integrated methodology combining MLFF and DFT. Moreover, since the calculation of reaction mechanisms still relies heavily on DFT, extending

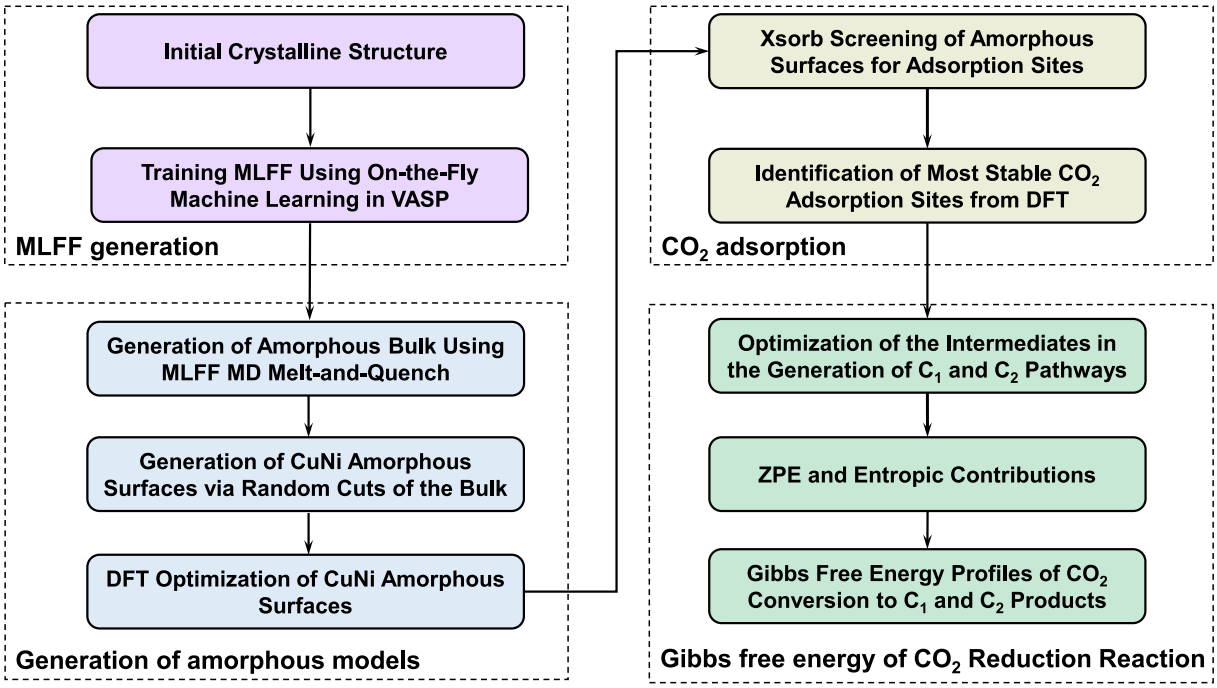

Fig. 1. Workflow of the methodology used to model the electrochemical CO_2 reduction on amorphous CuNi catalysts.

these computations across a wide range of Cu/Ni compositions would be computationally prohibitive. The use of MLFFs to compute the adsorption energetics of CO_2 on CuNi surfaces was also tested. However, inconsistent values of the adsorption energy compared to DFT were observed. These discrepancies could arise from limitations in the local energy description within the second-generation MLFF implementation in VASP.

2.2. Generation of the MLFF and DFT calculations

Spin-polarized DFT calculations were carried out within the projector augmented wave method [46] together with the Perdew-Burke-Ernzerhof (PBE) exchange correlation functional [47] and the Grimme's-D3 dispersion correction [48]. For the optimization of crystalline and amorphous surfaces, as well as their interaction with CO_2RR and HER intermediates, calculations employed a plane-wave cutoff of 400 eV, a $5 \times 5 \times 1$ Monkhorst-Pack *k*-point mesh for Brillouin zone sampling, and a convergence criterion of 10^{-4} eV Å^{-1} for the forces acting on each atom. The Bader Charge Analysis, developed by Henkelman's group, was used for charge analysis [49–51].

The MLFF for CuNi was trained using "on-the-fly" machine learning method implemented in version VASP [44,52,53]. During the MLFF generation procedure, MD simulations were conducted using a 2 fs time step in the NPT ensemble, using a Langevin thermostat and Parrinello-Rahman barostat. MLFF training was performed using a $(4 \times 3 \times 3)$ supercell of the CuNi bulk structure (orthorhombic, *Cmmm*, Material ID: mp-1225695) containing 144 atoms. For the DFT component of the MLFF training, a single *k*-point (gamma) was used along with a plane-wave cutoff of 550 eV. The system was gradually heated from 100 to 2700 K for 100,000 steps with a timestep of 2 fs with a fixed-shape volume fluctuation. For the MLFF generation, the VASP default values were used for the cutoff radius for radial and angular local atomic descriptors. Other MLFF hyperparameters were kept to the default VASP values. The accuracy of the generated MLFF was monitored by checking the root mean square errors (RMSE) of the energies and forces, which were constrained to be less than 5 meV atom^{-1} and 100 meV Å^{-1}, respectively. The comparison of the radial distribution function (RDF) of bulk CuNi at temperatures ranging from 300 to 2100 K, obtained from ab initio MD and MLFF MD trajectories, which are presented in Fig. S1 of the Supporting Information (SI), shows very good agreement, thus validating the MLFF. We also attempted to generate a MLFF to model CO_2 adsorbed on CuNi surfaces, but the binding energies were significantly different compared to DFT, likely due to the well-known deficiency of 2nd generation MLFFs, such as the one developed in VASP, which are "short-sighted". The typical cutoff radii for generating local atomic descriptors enclose only the first few coordination shells [54]. This approach was very successful for predominantly covalent and metallic materials; however, it reaches its limits when long-range interactions, such as the physisorption of molecules to surfaces, became important. Therefore, MLFF was primarily employed for generating an amorphous model due to its computational efficiency, while subsequent adsorption of CO_2 and CO_2RR intermediates was performed using DFT.

2.3. Generation of bulk and surface models of amorphous CuNi

The MLFF was used to generate the bulk structure of amorphous CuNi (*a*-CuNi) via the "melt-quench" method [30,31,55,56]. The initial structure was a $(4 \times 3 \times 3)$ supercell containing 144 CuNi atoms. Using the MLFF, this supercell underwent a series of NPT simulations, each lasting 40 ps. Target temperatures were set at 300 K intervals, ranging from 2700 down to 300 K. Finally, at 300 K, the system was equilibrated (production phase) for 20 ps to obtain a room-temperature amorphous phase structure.

A significant advantage of MLFF lies in their computational efficiency for conducting MD simulations [31,57]. For instance, performing the "melt-and-quench" simulation on a 144 atoms system using DFT would have required several weeks. In contrast, MLFFs completed these calculations within a fraction of the time (a few hours) while maintaining a comparable level of accuracy. Surface models were generated by cutting the CuNi amorphous bulk structure at four arbitrary planes, resulting in diverse surface morphologies: *a*-CuNi(i), *a*-CuNi(ii), *a*-CuNi(iii), and *a*-CuNi(iv). This

approach was used due to different surface terminations exposing varying quantities of undercoordinated atoms hence different types of densities of active sites. Exploring multiple surface configuration increases the probability of identifying those with optimal catalytic activity. These surface structures were initially optimized using the MLFF and then refined at DFT level.

2.4. Screening of CO_2 adsorption on amorphous CuNi surfaces using Xsorb

The Xsorb code [37,58] was used to screen the amorphous CuNi surface for stable CO_2 adsorption sites. Starting from the DFT-optimized structures of the CO_2 molecule and the *a*-CuNi surface (Fig. 2a), Xsorb systematically generated adsorption configurations by selecting potential sites based on a user-defined range of coordination numbers (CNs) of atoms (Fig. 2b). A preliminary screening step involved partial structural optimization of these configurations using DFT with reduced computational parameters (lower energy cut-off and a sparse *k*-point mesh) to speed up the process. Subsequently, full DFT optimizations were performed on the most stable adsorption configurations (those exhibiting favorable adsorption energies from the preliminary screening) using the higher energy cut-off and a denser *k*-point mesh values reported in Section 2.1 to achieve greater accuracy.

The generation of initial adsorption configurations with Xsorb involves the combination of adsorption sites and molecular rotations: a reference atom of the molecule is placed above the adsorption site, and the molecule is rotated pivoting around the reference atom (Fig. 2b, c). For the identification of the adsorption sites on amorphous surfaces, an ad hoc modification to the Xsorb code was implemented, since the original algorithm, based on high-symmetry sites, was aimed at crystalline surfaces. In the new procedure, the candidate sites are selected among the surface atoms within a depth Δz = 1.5 Å. For these atoms, the coordination number is computed. This can be done in Xsorb with several methods: (i) using a fixed cutoff radius for all atoms to count the nearest neighbors; (ii) using "natural cutoffs" based on covalent radii, where an atom is considered neighbour if its distance is less than the sum of covalent radii; (iii) employing a more sophisticated method (CrystalNN]) [59] optimized for inorganic crystal structures, based on the Voronoi algorithm and solid angles to determine the coordination environment. For this study, we used method (i), with a fixed cutoff radius of 1.5 Å. The adsorption sites are then selected according to their coordination number, including those below a threshold (here all sites with CN $\leq$ 10).

For the molecular rotations, instead of manually specifying the angles, the code was modified to include horizontal rotations of the molecule towards surrounding atoms, aiming to test "bridge" configurations where two atoms of the molecule adsorb on two neighboring atoms (Fig. 2c). More specifically, an oxygen atom of the CO_2 molecule was chosen as the reference atom to be placed on the main adsorption sites. Then, the molecule was rotated so that the O–C–O axis was pointing toward the neighboring atoms. These neighboring atoms include other main adsorption sites, plus other first nearest neighbors that were not selected as main sites, as visible in Fig. 2b. Finally, the molecule was also placed vertically on both main and surrounding sites, to test the interaction between a single oxygen of the CO_2 molecule and the substrate.

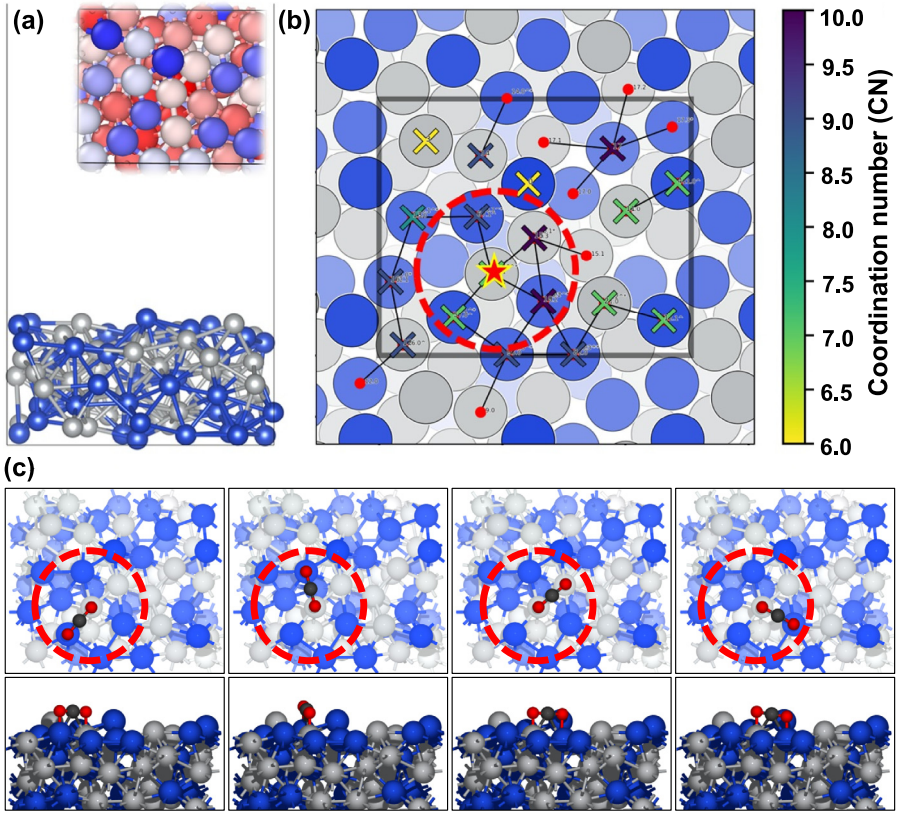

Fig. 2. (a) Side view of the amorphous CuNi surface labelled *a*-CuNi(i) with a top view color-coded representation of the highlighting atoms with different coordination numbers (CNs). The visualization illustrates the structural heterogeneity characteristic of the amorphous alloy, with distinct CN values assigned to each atom type. (b) The screening image of the *a*-CuNi(i) surface generated by Xsorb based on CN. (c) Top and lateral views of the initial adsorption configurations generated by rotations of the CO_2 molecule around the adsorption site marked with a star in (b). The O–C–O axis is oriented towards the neighbouring atoms.

2.5. Modelling electrochemical reactions

The solution-phase Gibbs free energies (G) of intermediates involved in the CO_2RR and HER pathways were calculated at the DFT level of theory using the following equation

$$G = E_e + \delta E_{ZPE} - TS \quad (1)$$

where the first term represents the total DFT electronic energy of the intermediate, incorporating hydration effects through the VASPsol implicit solvation model [60,61], ZPE denotes the zero-point energy correction, and TS is the entropic contribution at T = 298.15 K. Zero-point energies and entropies were determined within the harmonic approximation by evaluating vibrational frequencies of adsorbates and molecules using DFT calculations. The influence of pH and electrode potential (U) on reaction energy (ΔG) is accounted for using the following equation [62]

$$\Delta G = \Delta E_e + \Delta\delta E_{ZPE} - T\Delta S + \delta G_{pH} + \delta G_U \quad (2)$$

where the fourth term is the free energy correction arising from difference in proton concentration, $\delta G_{pH} = 2.303 k_B T$pH, and the last term is free energy correction due to the variation in electrode potential, $\delta G_U = -neU$, where n is the number of transferred electrons and e is the electronic charge. For this study, it was assumed that pH = 0 and U = 0. The PCET steps within CO_2R and HER were investigated using the Nørskov's computational hydrogen electrode (CHE) model [62]. This model offers an efficient approach to study PCET without explicitly considering protons and is widely used in theoretical electrocatalysis studies. Within the CHE model, zero voltage is defined based on the potential energy (μ) of components involved in the reversible hydrogen electrode across all pH, and T conditions: $\mu(H^+)$ + $\mu(e^-)$ = 1/2$\mu(H_2)$. This methodology was employed to calculate the ΔG values for elementary reactions listed in Table 1 involved in the formation of C_1 and C_2 products. The limiting potential (U_L) is defined by the following equation

$$U_L = -\Delta G_{PDS}/ne \quad (3)$$

where ΔG_{PDS} is the Gibbs free energy of the potential determining step (PDS) in the CO_2RR, namely, the PCET step with the largest free energy change. The overpotential (η) of the CO_2R (or HER) on a catalyst is determined by the difference between the equilibrium (U_{eq}) and limiting potentials

$$\eta = U_{eq} - U_L \quad (4)$$

The limiting potential (U_L) and the overpotential (η) serve as important parameters for assessing the catalytic activity towards CO_2R or HER [63]. Lower catalytic performance for a specific reaction is typically associated with higher overpotential, and vice versa. Finally, the adsorption of CO_2 on the Cu-Ni surface was calculated using the following equation

$$\Delta E_{CO_2} = E[(Cu)\cdots CO_2] - E(CO_2) - E(Cu) \quad (5)$$

where the first term represents the total energy of CO_2 adsorbed on the catalyst, and the second and third terms are the energies of the isolated CO_2 molecule and of the catalyst surface, respectively. A negative value of ΔE_{CO_2} indicates a favorable CO_2 adsorption.

Table 1
Elementary steps (PCET and C–C coupling) involved in the electrocatalytic CO_2 reduction to the C_1 products HCOOH and CO, and to the C_2 product C_2H_5OH and C_2H_4.

HCOOH	
$^* + CO_2 + H^+ + e^- \rightarrow {}^*OCHO$	(6)
$^*OCHO + H^+ + e^- \rightarrow HCOOH$ (l)	(7)
CO	
$^* + CO_2 + H^+ + e^- \rightarrow {}^*COOH$	
$^*COOH + H^+ + e^- \rightarrow {}^*CO + H_2O$	(8)
$^*CO \rightarrow {}^* + CO$ (g)	(9)
C_2H_5OH	
$^*CO + H^+ + e^- \rightarrow {}^*CHO$	(10)
$^*CO + {}^*CHO \rightarrow {}^*COCHO$	(11)
$^*COCHO + H^+ + e^- \rightarrow {}^*OCHCHO$	(12)
$^*OCHCHO + H^+ + e^- \rightarrow {}^*OCH_2CHO$	(13)
$^*OCH_2CHO + H^+ + e^- \rightarrow {}^*OHCH_2CHO$	(14)
$^*OHCH_2CHO + H^+ + e^- \rightarrow {}^*CH_2CHO + H_2O$	(15)
$^*CH_2CHO + H^+ + e^- \rightarrow {}^*CH_2CHOH$	(16)
$^*CH_2CHOH + H^+ + e^- \rightarrow {}^*CH_2CH_2OH$	(17)
$^*CH_2CH_2OH + H^+ + e^- \rightarrow {}^*CH_3CH_2OH$	
CH_2CH_2	
$^*CO + H^+ + e^- \rightarrow {}^*CHO$	(18)
$^*CO + {}^*CHO \rightarrow {}^*COCHO$	(19)
$^*COCHO + H^+ + e^- \rightarrow {}^*OCH_2CO$	(20)
$^*OCH_2CO + H^+ + e^- \rightarrow {}^*OCH_2COH$	(21)
$^*OCH_2COH + H^+ + e^- \rightarrow {}^*OCH_2CHOH$	(22)
$^*OCH_2CHOH + H^+ + e^- \rightarrow {}^*OCH_2CH + H_2O$	(23)
$^*OCH_2CH + H^+ + e^- \rightarrow {}^*OCH_2CH_2$	(24)
$^*OCH_2CH \rightarrow {}^*O + CH_2CH_2$	(25)

3. Results and discussion

3.1. Bulk and surface structural characterization

The crystalline (Fig. 3a) and amorphous (Fig. 3b) structures of the 1:1 CuNi alloy were characterized using their radial distribution function (RDF), in Fig. 3c, and angular distribution function (ADF), in Fig. 3d. The disordered nature of this amorphous structure is evident in the broadened peaks in both RDF and ADF compared to its crystalline counterpart, which arise from the loss of medium-to-long-range order in the amorphous structure. Furthermore, the crystalline nature of the *c*-CuNi bulk is evident by the distinct peaks of the Cu-Cu, Cu-Ni, and Ni-Ni, indicative of atomic ordering (Fig. 3f). The presence of a Cu-Ni peak at 3.5 Å (Fig. 3f) after the first coordination shell, highlights the defined atomic arrangement within the crystalline lattice. In contrast, for *a*-CuNi the RDFs highlight the absence of long-range (Fig. 3e), as evidenced by the significant overlap and broadening of their respective peaks. The inherent disorder within the amorphous structure enhances catalytic activity as discussed further below.

Unlike crystalline materials, which have defined surface orientations, amorphous structures lack crystal ordering, making this process more complex. Following Tilocca's protocol for modelling silicate glass surfaces [64], four different surfaces were generated from random cuts of the bulk *a*-CuNi structure, labelled (i–iv). Compared to the crystalline CuNi(111) surface (Fig. 4a), the amorphous CuNi surface (Fig. 4b) exhibits a significantly broader distribution of coordination numbers (CNs). On the crystalline surface, the atomic arrangement is uniform, with Cu atoms consistently showing a CN of 8 (Fig. 4c) and Ni atoms a CN of 9 (Fig. 4d). In contrast, the amorphous CuNi surface displays substantial variability, with CNs ranging from 6 to 13 for Cu atoms and from 5 to 14 for Ni atoms (Fig. 4e, f). This trend is also observed across other amorphous surfaces (Fig. S2), with corresponding CN distributions shown in Fig. S3, confirming that such diversity is a general characteristic of amorphous structures. The wide range of coordination environments in the amorphous phase is likely to influence catalytic activity by introducing a variety of active sites with distinct electronic and geometric properties. Interestingly, the surface energies in Table S1 of the amorphous surfaces, ranging from 0.241 to 0.250 eV Å^{-2}, are comparable to that of the crystalline CuNi(111) surface (0.262 eV Å^{-2}). This suggests slightly lower surface energies and potentially greater surface stability for the amorphous surfaces.

Moreover, the crystalline and amorphous phases of the Cu-rich 3:1 CuNi alloy were also generated using the same MLFF developed for the 1:1 system. The RDF profile (Supporting Information,

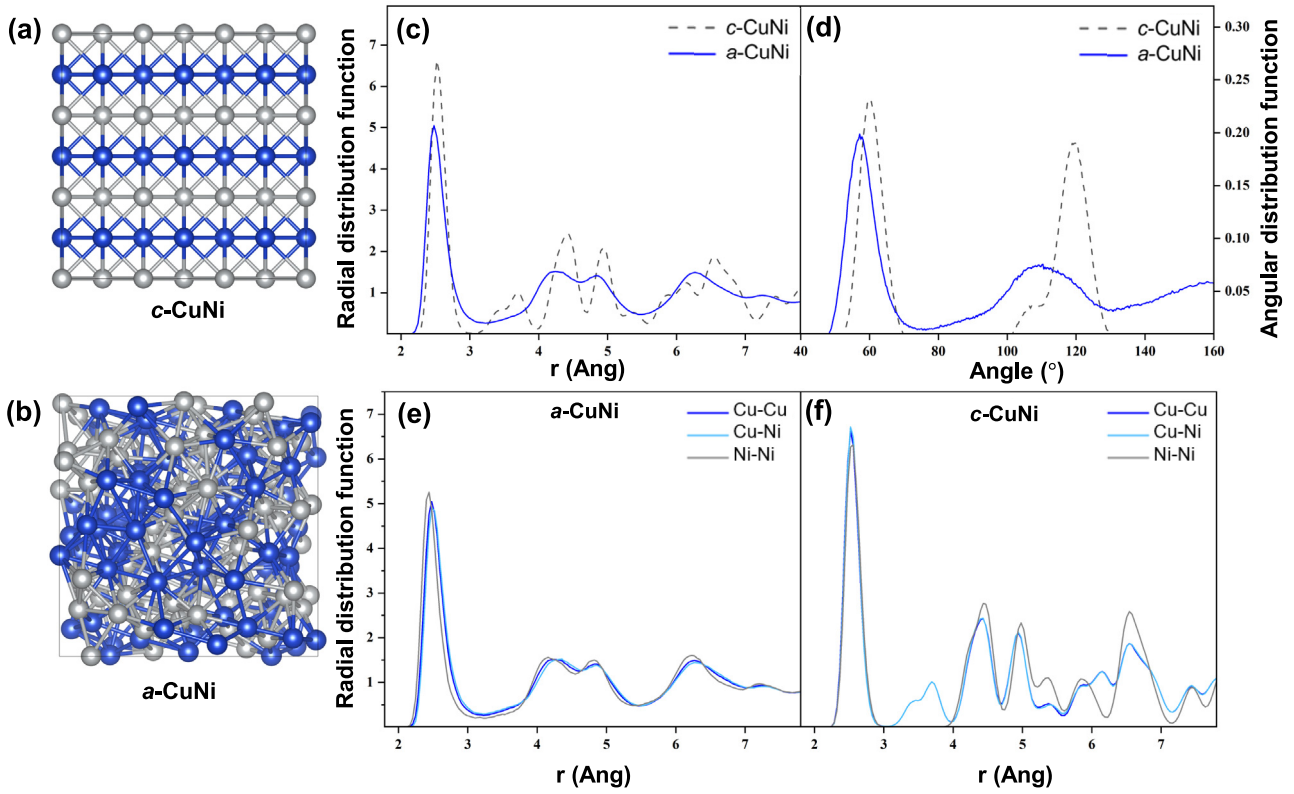

Fig. 3. Optimized bulk structures of (a) crystalline and (b) amorphous CuNi alloys. (c) Radial distribution functions (RDFs) and (d) angular distribution functions (ADFs) of the crystalline and amorphous CuNi structures, computed from MLFF MD simulations at 300 K. (e) Pair-specific RDFs for Cu–Cu, Cu–Ni, and Ni–Ni interactions in (e) amorphous CuNi (*a*-CuNi) and (f) crystalline CuNi (*c*-CuNi) alloys.

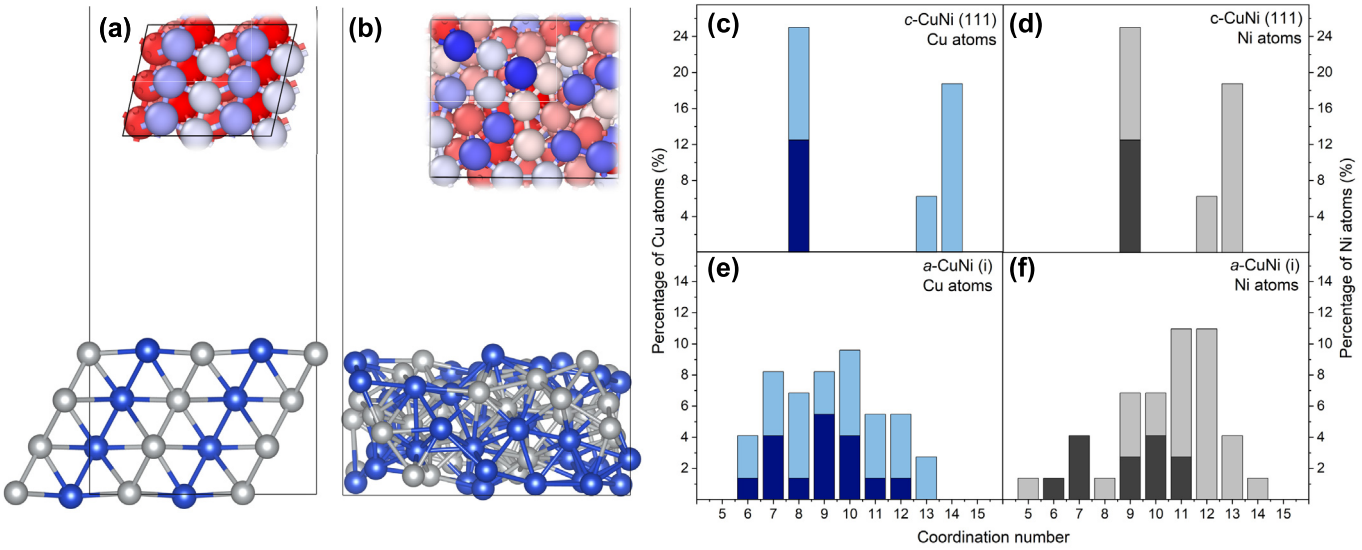

Fig. 4. Structures of (a) the crystalline CuNi(111) surface and (b) the amorphous CuNi surface labelled *a*-CuNi(i), with a color-coded image representing the coordination number (CN) on their surfaces. CN analysis of (c) Cu atoms and (d) Ni atoms on the crystalline CuNi(111) surface, as well as (e) Cu atoms and (f) Ni atoms on the *a*-CuNi(i) surface. Lighter bars indicate the CN of all atoms in the surface model, while darker bars represent the CN of the surface atoms. Similar behaviour is observed for the surfaces of amorphous CuNi labeled (ii)–(iv), which are detailed in the Supporting Information (Fig. S3).

Fig. S1) shows the expected signatures of ordered and disordered structures, consistent with those observed for the 1:1 composition. The ability of the MLFF to accurately reproduce the characteristic peak positions for both crystalline and amorphous phases at this different composition highlights its transferability to CuNi alloys beyond the training ratio. This demonstrates that the framework can be applied directly to other alloy stoichiometries, enabling efficient exploration of compositional effects on structural and catalytic properties for future work.

In transition metals such as Cu and Ni, the outermost *d* electrons form an energy band known as the *d*-band. The *d*-band center, representing the average energy of *d* electrons, influences the

interaction strength between the metal and adsorbed molecules, particularly based on its position relative to the Fermi level [65]. When the *d*-band center is positioned closer to the Fermi level, the metal surface tends to form stronger bonds with adsorbates such as CO_2, due to enhanced orbital hybridization and increased electron back-donation, which facilitate the activation of the adsorbed molecule. The *d*-band centers of the amorphous surfaces range from –1.54 to –1.60 eV, comparable to that of the crystalline surface (–1.53 eV). In our previous study on pure Cu amorphous surfaces, the *d*-band center values ranged from –2.37 to –2.43 eV, while those for crystalline Cu(100) and Cu(111) were –2.45 and –2.28 eV, respectively [29]. Thus, Ni-alloying shifts the *d*-band center closer to the Fermi level, an observation consistent with the finding of Ou et al, who reported an upshift in the *d*-band center for Ni doped Cu(111) compared to the pure Cu(111) [66]. Similarly, Tang et al. showed that alloying Cu into Ni down-shifted the *d*-band centre from –1.37 eV in Ni(111) to –1.53 eV in Ni_3Cu(111) [67].

3.2. CO_2 adsorption and activation

While crystalline CuNi(111) shows stronger overall CO_2 adsorption than amorphous CuNi, the latter still exhibits favorable chemisorption energies between –0.28 and –0.70 eV. The optimized structures for CO_2 adsorption are shown in Fig. 5 and Fig. S4. Notably, the strength of CO_2 adsorption on the amorphous surface is highly site dependent. Low-coordinated Ni sites (CN between 6 and 7) demonstrate the strongest CO_2 adsorption, with chemisorption energies of –0.70 eV and physisorption energies of –0.81 eV (Table 2). This is further supported by the Ni *d*-band center being closer to the Fermi level (–1.32 eV for Ni compared to –2.09 eV for Cu), indicating higher affinity towards CO_2. The results also suggest a synergistic effect of neighboring undercoordinated Cu and Ni (CN = 7), where both Cu and Ni exhibit enhanced CO_2 chemisorption and activation (adsorption energies between –0.59 to –0.70 eV) compared to higher coordinated sites (CN = 10) with adsorption energies between –0.28 to 0.30 eV. This highlights the importance of low-coordinated environments in promoting CO_2 adsorption on the amorphous CuNi. surface.

The *a*-CuNi(i) amorphous surface was selected for detailed investigation due to its unique structural features: undercoordinated Cu and Ni atoms with coordination numbers (CN) of 6, and three distinct Cu–Ni pairs with CN = 7. This specific arrangement, absent in other amorphous surfaces, is considered critical for catalytic performance. For comparison, CO_2 adsorption was also evaluated on *a*-CuNi(ii), with results summarized in Table S2. Strong adsorption was observed, with chemisorption energies ranging from –1.31 to –2.19 eV and physisorption energies from –0.84 to –1.59 eV. While this indicates effective CO_2 activation, such strong binding may hinder intermediate desorption or transformation, potentially limiting the formation of C_1 and C_2 products.

3.3. Electrochemical CO_2 reduction to C_1 products

The Gibbs free energy profiles for the CO_2RR to CO and HCOOH are presented in Fig. 6a and b, respectively. The optimized structures of the intermediates involved in the formation of CO and HCOOH are shown in Fig. S5. Since the CO_2RR competes with the HER, this reaction was also considered. From the free energy profiles, the value of ΔG_{PDS} was used to determine the overpotentials associated with the CO_2RR leading to either HCOOH or CO, as well as for the HER producing H_2 (Fig. 6d). Three active sites on the *a*-CuNi (i) surface, shown in Fig. 6e, were selected: site A corresponds to the most favorable chemisorption site (ΔE_{CO_2} = –0.70 eV); site B corresponds to the most favorable physisorption site (ΔE_{CO_2}= –0.81 eV) at an undercoordinated Ni atom; site C is the only site with an undercoordinated Cu atom (CN = 6) and favorable CO_2 physisorption (ΔE_{CO_2} = –0.25 eV). For comparison, the CO_2 conversion to CO and HCOOH was also studied on the crystalline CuNi (111) surface (Fig. 6f).

The first striking difference between amorphous and crystalline CuNi is the significantly lower overpotential, which enhances the catalytic activity of amorphous CuNi surfaces compared to the (111) surface for both CO_2RR and HER. On the CuNi(111) surface, all intermediates are strongly bound, resulting in a high overpotential. Moreover, the stability of these intermediates varies considerably on the amorphous CuNi surface, depending on the reaction site. Specifically, site C exhibits the highest catalytic activity, followed by site A.

The partial density of states analysis (PDOS) of Cu and Ni *d*-orbitals on the amorphous CuNi surface (Fig. 6g, i) and crystalline CuNi(111) (Fig. 6h, j) surfaces reveal distinct electronic structure modifications induced by amorphization. While crystalline CuNi (111) exhibits well-defined *d*-band for both Cu and Ni (Fig. 6h, j), the amorphous CuNi(i) surface (Fig. 6g, i) displays significant degree of orbital overlap. This can be attributed to the distorted geometry and varying coordination environments within the amorphous structure, leading to reduced symmetry and consequently, reducing the splitting of the *d*-orbitals. This phenomenon aligns with crystal field theory, where variations in coordination number weaken the ligand field, reducing the energy difference between t_{2g} and e_g orbitals and ultimately promoting orbital overlap. This effect is likely to contribute to the observed site dependent energetics of CO_2RR to CO and HCOOH on *a*-CuNi (Fig. 6a, b). Wang et al. also reported a similar observation of *p*-*d* orbital merging in amorphous $RuTe_2$ [25]. The authors attributed this to the distorted nature of the amorphous system, which minimizes the effect of crystal field splitting, leading to increased orbital overlap and enhanced electron exchange between *p* and *d* orbitals influencing its catalytic activity [25]. The hybridization of *d*-orbitals in *a*-CuNi leads to the formation of new regions of electron density on the surface, which influence adsorbate interaction and catalytic behaviour. In addition, PDOS reveals that the Ni *d*-band centre lies closer to the Fermi energy level compared to Cu in both crystalline and amorphous CuNi, suggesting stronger Ni and

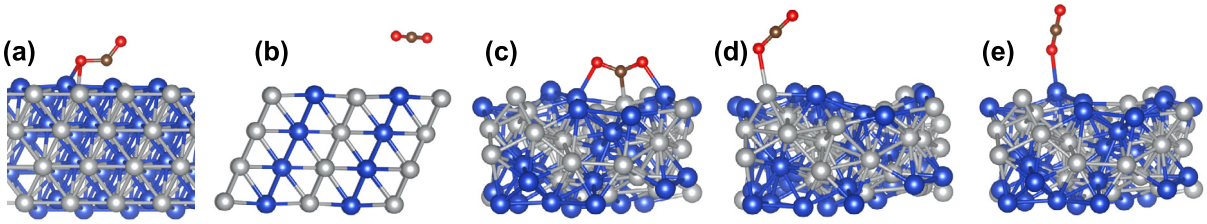

Fig. 5. CO_2 adsorption on CuNi: (a) Chemisorption on the crystalline CuNi(111) surface; (b) Physisorption on the crystalline CuNi(111) surface; (c) Chemisorption on the amorphous CuNi surface; (d) Physisorption on the Ni site of the amorphous CuNi surface; (e) Physisorption on the Cu site of the amorphous CuNi surface labelled *a*-CuNi(i).

Table 2
Coordination number (CN) of the Cu and Ni active sites, adsorption energy (ΔE_{CO_2}, in eV), C–O bond length (d_{C-O}, in Å), O–C–O bond angle (θ_{OCO}, in degrees), and charge transfer (ΔQ, in e) of CO_2 adsorbed on the crystalline CuNi(111) and the amorphous CuNi surface labelled *a*-CuNi(i).

System	CN		ΔE_{CO_2}	d_{C-O}	θ_{OCO}	ΔQ
	Cu	Ni				
***c*-CuNi(111)**						
Chemisorption	8	9	−1.88	1.33,1.22	128.7	−0.79
	–	9, 9	−1.68	1.24,1.25	139.2	−0.67
Physisorption	8	–	−1.73	1.18,1.18	179.7	−0.05
	–	9	−1.64	1.18,1.18	179.5	−0.05
	–	9	−1.63	1.18,1.18	179.5	−0.05
***a*-CuNi**						
Chemisorption	7, 9	7	−0.70	1.26,1.27	130.7	−0.76
	7	7	−0.64	1.24,1.25	142.3	−0.60
	7	7	−0.60	1.24,1.24	141.6	−0.62
	7	7	−0.59	1.22,1.28	135.5	−0.63
	–	7, 10	−0.30	1.23,129	134.6	−0.69
	–	7, 10	−0.28	1.25,1.21	145.2	−0.50
Physisorption	–	6	−0.81	1.18,1.17	179.7	−0.04
	–	7	−0.30	1.18,1.17	179.6	−0.03
	8, 9	–	−0.27	1.18,1.18	179.7	−0.06
	–	7	−0.26	1.18,1.17	179.5	−0.04
	6	–	−0.25	1.18,1.17	179.9	−0.01

adsorbate interaction. This aligns with the observed stronger binding of intermediate observed for crystalline CuNi(111) surface for CO and HCOOH formation (Fig. 6a, b), where the active sites consist of mainly Ni atoms (Fig. 6f). In the amorphous phase, the presence of undercoordinated Cu and Ni atoms, coupled with the synergistic effects arising from *d*-orbital hybridization, is expected to modulate reaction energetics and enhance catalytic activity towards CO_2 reduction.

Given the critical role of CO as an intermediate in the formation of C_2 products, the CHE model (Eq. (2)) was employed to assess the influence of pH on the conversion of CO_2 to CO (see Fig. S10). The results indicate that alkaline conditions (pH > 7) are more favorable for CO production, suggesting that elevated pH enhances the reaction environment for CO_2 reduction to CO. However, on crystalline CuNi(111) surfaces, the strong adsorption of reaction intermediates may significantly hinder CO desorption, making the CO_2-to-CO conversion both thermodynamically and kinetically less favorable compared to amorphous surfaces.

In previous studies, N-doped carbon-supported CuNi bimetallic catalysts with alloy (CuNi/NC-alloy) and phase-separated (CuNi/NC-PS) structures have been reported, along with their respective Gibbs free energy profiles for the CO_2 to CO conversion [36]. For the CuNi/NC-PS catalyst, a *d*-band center of −1.74 eV was observed. In contrast, our amorphous CuNi surfaces exhibit a *d*-band centre ranging from −1.54 to −1.60 eV, which is closer to the Fermi level, thus enhancing CO_2 adsorption and activation. In their study, the rate-determining step was identified as CO desorption, with corresponding Gibbs free energy changes of 1.15 and 0.89 eV for the CuNi/NC-alloy and CuNi/NC-PS catalysts, respectively, which was attributed to strong CO adsorption on Ni sites [36]. In comparison, the amorphous *a*-CuNi(i) surface has a lower CO desorption energy of 0.75 eV. Similarly, Yun et al. conducted DFT calculations on CuNi decorated N-doped carbon substrates (CuNi/NC) for CO_2-to-CO conversion [68]. The authors reported a free energy of 0.71 eV for the formation of *COOH on the CuNi(111) crystalline surface. Our results show a slightly lower value of 0.63 eV, suggesting more favorable intermediate formation on the amorphous surface. Furthermore, CO desorption energy was calculated to be 1.21 eV on their crystalline surface, which is notably higher than on our amorphous model, again highlighting the improved desorption characteristics of the latter. Additionally, Zhang et al. explored the effect of Ni cluster decoration on defect-rich Cu surfaces. Their study revealed that Ni incorporation enhances the adsorption of $*CO_2$, *COOH, and *CO intermediates, as evidenced by a more favourable Gibbs free energy profile [69]. However, specific values for adsorption energies and CO desorption were not reported, limiting direct comparison. Unlike these prior studies on CuNi, our investigation extends beyond the formation of CO. In the following section, the electrochemical reduction of CO to higher-value C_2 products such as ethanol and ethylene on both amorphous and crystalline surfaces is examined.

3.4. Electrochemical CO_2 reduction to C_2 products

The electrocatalytic conversion of CO_2 to ethanol and ethylene was investigated on both amorphous and crystalline CuNi surfaces by computing the CO···CHO coupling mechanism for C_2 product formation in Fig. 7a, b proposed by Garza et al. [13]. The structure of the intermediates involved in the formation of ethanol and ethylene on the crystalline and amorphous CuNi surfaces is presented in Fig. S6. Xsorb was used to identify reactive sites for the *COCHO intermediate on the amorphous surfaces, revealing stable adsorption near the reactive sites B and C in Fig. 6e. At these sites, *COCHO is bonded to the undercoordinated Cu and Ni atoms (CN = 6). The undercoordination of both Cu and Ni atoms is likely to result in a higher local charge density, which, combined with the intrinsically lower *d*-band center of Ni relative to Cu, is expected to promote synergistic interactions between adjacent Cu and Ni atoms.

While the undercoordinated Cu–Ni configuration observed on the *a*-CuNi(i) surface, such as adjacent Cu and Ni atoms both with a CN of 6, represents a potentially highly active catalytic site, its occurrence is not guaranteed across all amorphous surface configurations. However, due to the inherent structural disorder of amorphous alloys, such motifs are likely to emerge with some regularity. This suggests that the synergistic Cu–Ni interaction is not a rare or isolated feature, but rather a representative catalytic motif that may appear, with varying frequency, across a broader range of *a*-CuNi surface models.

This electronic modification is likely to enhance the activation of *COCHO and facilitate subsequent reaction steps, leading to the favorable energetics observed in Fig. 7c. Consequently, the *a*-CuNi surface exhibits a significantly lower Gibbs free energy for the CO···CHO coupling (ΔG = 0.04 eV) compared to the crystalline CuNi(111) surface (ΔG = 1.57 eV in Fig. 7d). A key structural difference is the binding configuration of *COCHO: the oxygen atoms bind to both Cu and Ni atoms on *a*-CuNi, but predominantly

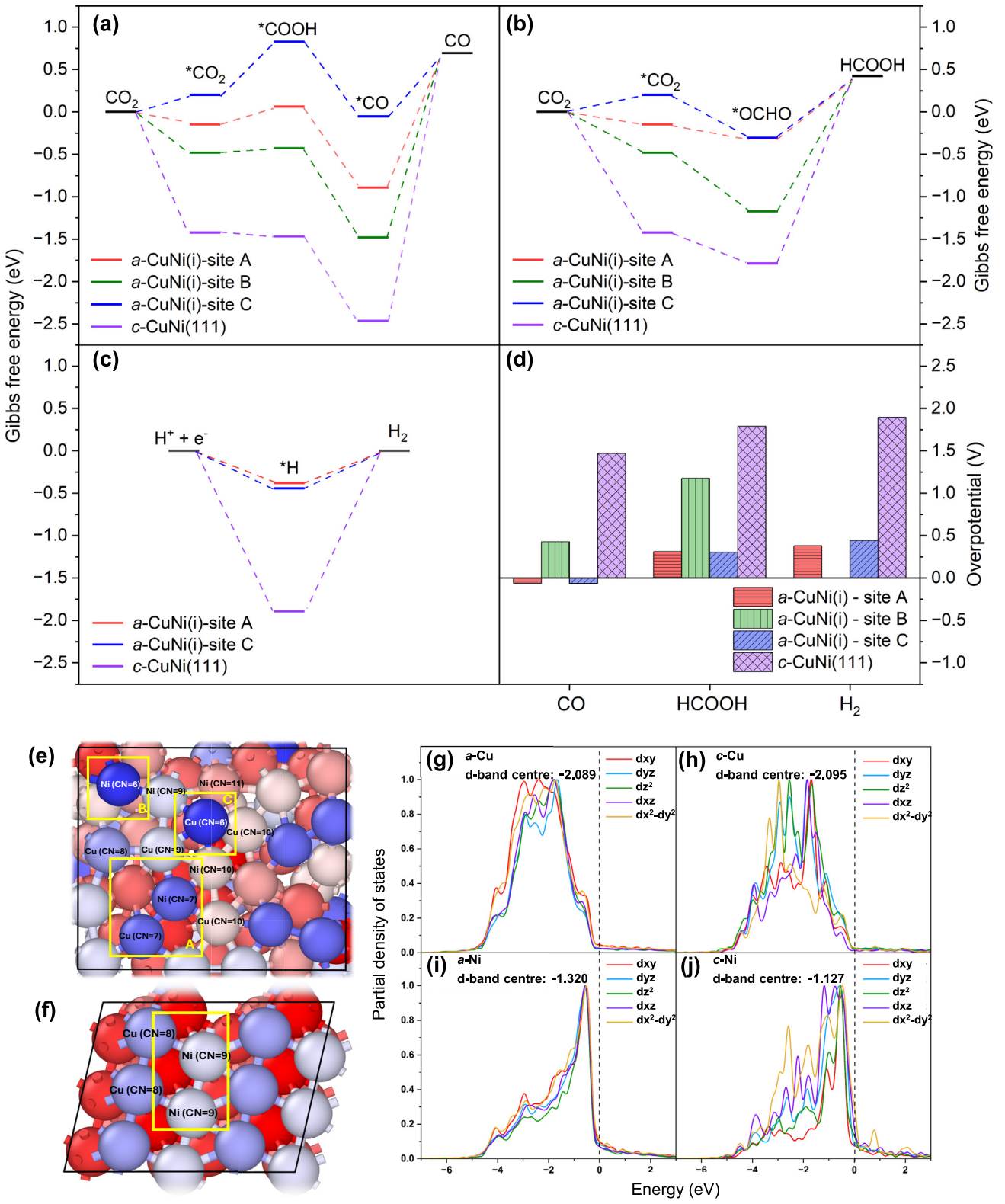

Fig. 6. Gibbs free energy profiles for the CO_2RR towards (a) CO and (b) HCOOH. (c) Gibbs free energy profile for the HER. (d) Overpotentials for CO_2RR and HER. The catalytic active sites (e) on the amorphous CuNi surface and (f) on the crystalline CuNi(111) surface labelled according to the coordination number (CN). Partial density of states (PDOS) of the Cu atoms (g) in the (h) amorphous CuNi surface and (i) crystalline CuNi(111) surface. PDOS of the Ni atoms in the (i) amorphous CuNi surface and (j) crystaline CuNi (111) surface.

to Cu atoms on CuNi(111) (Fig. S7). Bader charge analysis shows a higher positive charge of the Ni (+0.34 e) and Cu (+0.30 e) on the *a*-CuNi surface compared to both Cu atoms (approximately + 0.25e) on CuNi(111) surface involved in the *COCHO bonding, indicating greater electron transfer from Ni to O and relatively a stronger Ni–O bond (Fig. S7).

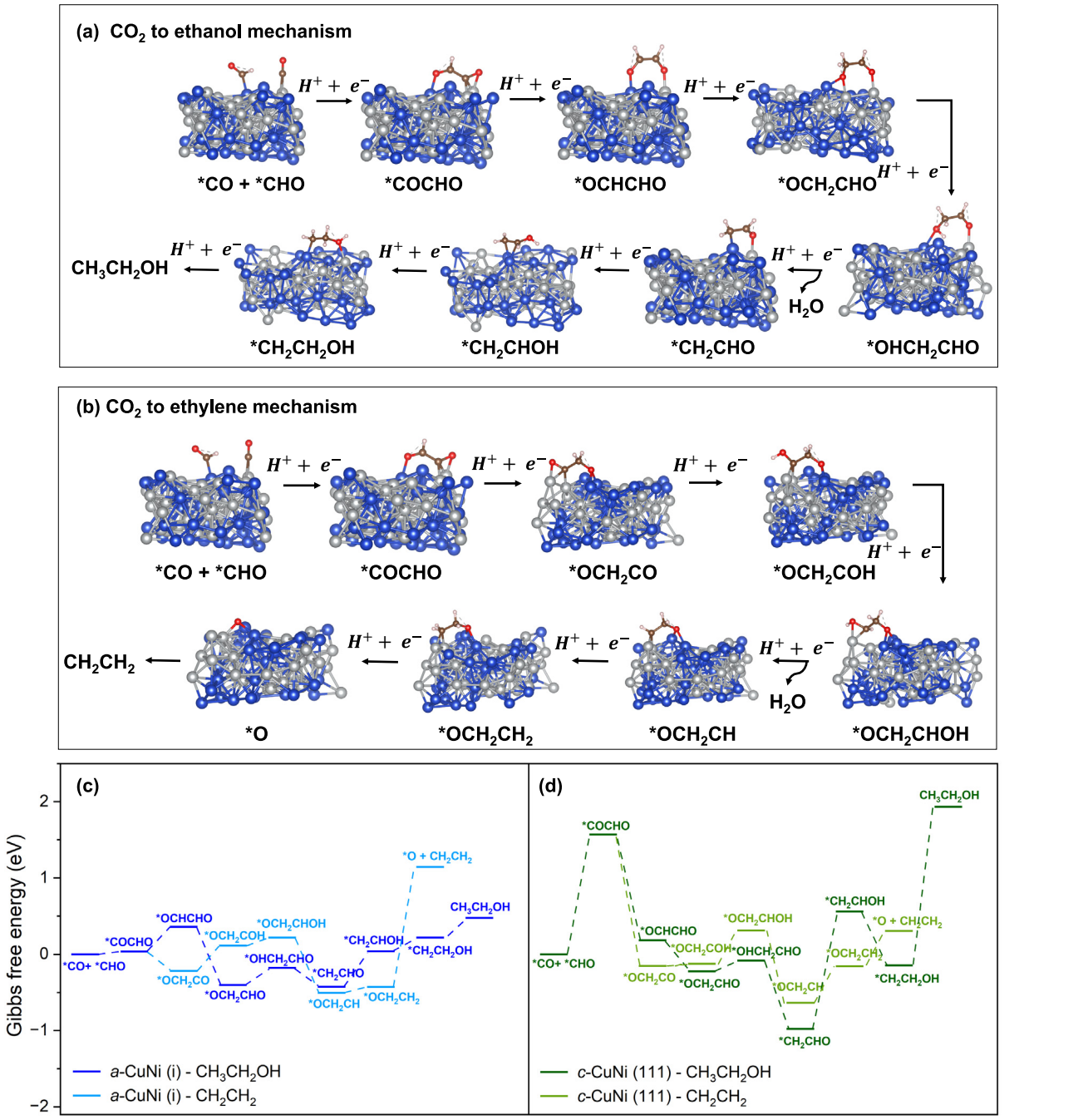

Fig. 7. Optimized structures of the intermediates involved in the CO_2 reduction to (a) ethanol (C_2H_5OH) and (b) ethylene (C_2H_2). Gibbs free energy profiles for the CO_2 reduction towards C_2H_5OH and C_2H_2 on (c) the amorphous CuNi surface and (d) the crystalline CuNi(111) surface.

The PDOS analysis (Fig. S8) reveals a higher density of Ni *d*-orbitals near the Fermi level, with the Ni *d*-band center positioned closer to the Fermi level than that of Cu (Fig. 6g–j). This electronic configuration suggests stronger hybridization between Ni *d*-orbitals and O 2*p* orbitals, due to more favorable orbital overlap compared to Cu. As a result, this enhanced interaction can lower the free energy barrier for *COCHO formation, potentially improving catalytic performance. Moreover, a significant difference in charge redistribution is observed between the amorphous and crystalline surfaces as revealed by the charge density difference plots (Fig. S9). On the amorphous surface (Fig. S9a, b), regions of electron accumulation and depletion are more pronounced and spatially localized around *COCHO, indicating stronger and more directional orbital interactions with the surface. This behavior reflects the inherent flexibility of the disordered atomic environment, which allows local orbital orientations to adjust and maximize overlap with the adsorbate. In contrast, the crystalline surface (Fig. S9c, d) exhibits more symmetric and delocalized charge redistribution patterns, suggesting that the periodic lattice constrains the orientation of surface orbitals and limits their ability to engage effectively with the intermediate. These findings show that structural disorder facilitates enhanced orbital overlap and charge transfer, leading to improved stabilization of reactive intermediates such as *COCHO. This highlights a key advantage of amorphous materials in catalytic applications, particularly for reactions involving complex adsorbates that benefit from flexible electronic environments. On amorphous CuNi, ethanol formation is favored over ethylene due to the lower Gibbs free energies of

key reaction intermediates, along with a notably low ethanol desorption energy of 0.26 eV (Fig. 7c).

While ethylene formation on amorphous CuNi also exhibits favorable energetics for its early intermediates, the strong adsorption of $*OCH_2CH_2$ significantly hinders its desorption as the final product (Fig. 7c). In contrast, on crystalline CuNi(111), the formation of C_2 products is limited by the initial coupling of *CO and CHO, as evidenced by the positive Gibbs free energy associated with COCHO formation (Fig. 7d), impeding the progression of the reaction pathway.

Furthermore, the analysis of subsequent reaction intermediates suggests a potential selectivity towards ethylene over ethanol on this surface. In Fig. 7d, while crystalline CuNi(111) exhibits a lower energetic barrier for $*OCH_2CH_2$ dissociation to form ethylene (0.46 eV) compared to the high barrier for the final hydrogenation step in ethanol formation (2.08 eV), the initial unfavorable coupling of *CO and *CHO remains a critical limiting step. Consequently, even considering the subsequent reaction energetics, the inherent difficulty in forming the initial C–C bond on crystalline CuNi(111) implies a limited overall catalytic performance for the CO_2 electrochemical reduction to C_2 products.

Zhang et al. synthesized defect-rich Cu nanowires decorated with uniformly dispersed Ni clusters via a coordination-enabled galvanic replacement method, ensuring controlled and homogeneous Ni distribution across the surface [69]. The resulting catalyst exhibited a disordered surface characterized by nanograins with mismatched lattice directions, indicative of a high density of defects and grain boundaries. The CuNi system, particularly with 0.82 % Ni doping, demonstrated superior selectivity for C_2 products, including ethanol and ethylene, achieving a FE of 44 % at −0.77 V vs RHE, which was sevenfold higher than that of pure Cu NWs (6.3 %) [69]. DFT studies revealed that Ni decoration on Cu facilitates the adsorption of $*CO_2$, *COOH, and *CO on Cu-Ni bridge atoms, significantly lowering energy barriers for intermediates and enhancing C–C coupling [69]. This aligns with our findings that Cu-Ni bridge atoms serve as the most favorable active sites for C–C coupling reactions. Furthermore, the formation of ethanol on *a*-CuNi is consistent with a previous study by Duan et al., in which amorphous Cu nanoparticles achieved a FE of 59 % for liquid fuels at −1.4 V, comprising 22 % ethanol and 37 % formic acid [26]. This highlights the potential of amorphous Cu-based catalysts for selective CO_2 reduction to valuable liquid products and suggests that the abundance of undercoordinated atoms in amorphous structures facilitates both C–C bond formation and PCET step, favoring ethanol production. Conversely, crystalline Cu systems, with their ordered surfaces, favor ethylene due to enhanced C–C coupling but limited hydrogenation. This observation is corroborated by Jayachandran et al., who reported higher FE for ethylene FE (16 % at −1.5 V vs RHE) on reheated crystalline Cu compared to amorphous Cu (7 % at −1.5 V vs RHE) [70], further reinforcing the influence of surface structure on product selectivity.

4. Conclusions

This study demonstrates computationally the superior performance of amorphous CuNi catalysts for CO_2 electrochemical reduction, leveraging machine learning forcefields for efficient structure generation and functional theory for subsequent refinement and property calculations. Undercoordinated Cu and Ni sites in the amorphous structure significantly enhance catalytic activity. Ni incorporation to Cu amorphous system lowered the *d*-band centre, while the disordered structure reduced *d*-orbital splitting, altering electronic properties. Our findings reveal that the undercoordinated sites facilitate the favourable formation of CO, a key intermediate in the generation of C_{2+} products. Furthermore, this study demonstrates a higher selectivity towards ethanol over ethylene on amorphous CuNi, as evidenced by the more thermodynamically favourable Gibbs free energy profile compared to that of the crystalline CuNi surface. The stronger Ni–O bond and favourable adsorption of the intermediate COCHO, supported by Bader charge and PDOS analysis, enhanced catalytic performance. Moreover, the amorphous catalyst consisting of high density of undercoordinated atoms are effective for both C–C bond formation and hydrogenation leading to ethanol production over ethylene. Future research should focus on optimizing the composition and morphology of amorphous bimetallic Cu-based catalysts to further enhance their performance and explore their applicability in practical CO_2 conversion systems.

Moreover, this work introduces a methodologically distinct framework that significantly broadens the scope of modelling multicomponent amorphous systems and their surface reactivity. Notably, the approach is not limited to CO_2 reduction reactions but is readily extendable to other electrocatalytic processes of interest, such as the oxygen evolution reaction, oxygen reduction reaction, nitrogen reduction reaction for which amorphous systems have also shown potential. This versatility underlines the potential of the method for broader application across various catalytic systems.

CRediT authorship contribution statement

Akshayini Muthuperiyanayagam: Writing – original draft, Methodology, Investigation, Formal analysis, Data curation, Conceptualization. **Enrico Pedretti:** Writing – review & editing, Software, Methodology, Conceptualization. **Maria Clelia Righi:** Writing – review & editing, Supervision, Project administration, Methodology, Funding acquisition, Conceptualization. **Devis Di Tommaso:** Writing – review & editing, Supervision, Project administration, Methodology, Funding acquisition, Conceptualization.

Declaration of competing interest

The authors declare that they have no known competing financial interests or personal relationships that could have appeared to influence the work reported in this paper.

Acknowledgements

We are grateful to the UK Materials and Molecular Modelling Hub for computational resources, which is partially funded by EPSRC (EP/T022213/1, EP/W032260/1 and EP/P020194/1) via our membership of the UK's HEC Materials Chemistry Consortium, which is funded by EPSRC (EP/L000202). This work used the ARCHER UK National Super-computing Service (https://www.archer.ac.uk). This research utilized Queen Mary's Apocrita HPC facility, supported by QMUL Research-IT (https://doi.org/10.5281/zenodo.438045). These results are part of the "Advancing Solid Interface and Lubricants by First Principles Material Design (SLIDE)" project that has received funding from the European Research Council (ERC) under the European Union's Horizon 2020 research and innovation program (Grant agreement No. 865633). Furthermore, D. D. T. thanks the Leverhulme Trust, United Kingdom (RPG-2023-239) for resources supporting projects advancing materials characterization by computational means.

Appendix A. Supplementary material

Supplementary data to this article can be found online at https://doi.org/10.1016/j.jechem.2025.08.089.

References

[1] J. Yan, W. Song, Z. Zhao, M. Zhang, Y. Wu, L. Zhang, Int. J. Hydrogen Energy 89 (2024) 664–685.
[2] C.A.R. Pappijn, M. Ruitenbeek, M.F. Reyniers, K.M. Van Geem, Front. Energy Res. 8 (2020) 557466.
[3] F. Wang, Z. Lu, H. Guo, G. Hao, W. Jiang, G. Liu, Coord. Chem. Rev. 515 (2024) 215962.
[4] C.P. O'Brien, R.K. Miao, A. Shayesteh Zeraati, G. Lee, E.H. Sargent, D. Sinton, Chem. Rev. 124 (2024) 3648–3693.
[5] Y. Hori, Electrochemical CO_2 reduction on Metal Electrodes, in: C.G. Vayenas, R.E. White, M.E. Gamboa-Aldeco (Eds.), Modern Aspects of Electrochemistry, Springer, New York, 2008, pp. 89–189.
[6] A.R. Woldu, Z. Huang, P. Zhao, L. Hu, D. Astruc, Coord. Chem. Rev. 454 (2022) 214340.
[7] H. Xie, T. Wang, J. Liang, Q. Li, S. Sun, Nano Today 21 (2018) 41–54.
[8] Z. Weng, J. Jiang, Y. Wu, Z. Wu, X. Guo, K.L. Materna, W. Liu, V.S. Batista, G.W. Brudvig, H. Wang, J. Am. Chem. Soc. 138 (2016) 8076–8079.
[9] E.W. Lees, B.A.W. Mowbray, F.G.L. Parlane, C.P. Berlinguette, Nat. Rev. Mater. 7 (2022) 55–64.
[10] J. Wu, Y. Huang, W. Ye, Y. Li, Adv. Sci. 4 (2017) 1700194.
[11] P. Wilde, P.B. O'Mara, J.R.C. Junqueira, T. Tarnev, T.M. Benedetti, C. Andronescu, Y.-T. Chen, R.D. Tilley, W. Schuhmann, J.J. Gooding, Chem. Sci. 12 (2021) 4028–4033.
[12] H. Ooka, M.C. Figueiredo, M.T.M. Koper, Langmuir 33 (2017) 9307–9313.
[13] A.J. Garza, A.T. Bell, M. Head-Gordon, ACS Catal. 8 (2018) 1490–1499.
[14] L. Ou, Z. He, Surf. Sci. 705 (2021) 121782.
[15] W. Xu, J. Chen, C. Liu, J. Xu, X. Wang, T. Li, J. Wang, R. Xiao, Appl. Catal. B 363 (2025) 124825.
[16] W. Choi, Y. Chae, E. Liu, D. Kim, W.S. Drisdell, H. Oh, J.H. Koh, D.K. Lee, U. Lee, D. H. Won, Nat. Commun. 15 (2024) 8345.
[17] D. Giziński, M. Najderek, A. Brudzisz, J. Lee, J. Choi, W.J. Stępniowski, Surf. Interfaces 44 (2024) 103692.
[18] Y. Yang, J. Evans, J.A. Rodriguez, M.G. White, P. Liu, Phys. Chem. Chem. Phys. 12 (2010) 9909–9917.
[19] Z. Chen, Z. Ma, G. Fan, F. Li, ACS Appl. Mater. Interfaces 16 (2024) 35143–35154.
[20] D. Wang, J. Wang, Z. Wang, N. Zhang, J. Zeng, H. Zhong, et al., Precis. Chem. 2 (2024) 96–102.
[21] W. Guo, J. Bi, Q. Zhu, J. Ma, G. Yang, H. Wu, et al., ACS Sustain. Chem. Eng. 8 (2020) 12561–12567.
[22] X. Chen, D.A. Henckel, U.O. Nwabara, Y. Li, A.I. Frenkel, T.T. Fister, et al., ACS Catal. 10 (2020) 672–682.
[23] J. Kang, F. Li, Z. Xu, X. Chen, M. Sun, Y. Li, et al., JACS Au 3 (2023) 2660–2676.
[24] V.V. Hoang, D. Ganguli, Phys. Rep. 518 (2012) 81–140.
[25] J. Wang, L. Han, B. Huang, Q. Shao, H.L. Xin, X. Huang, Nat. Commun. 10 (2019) 5692.
[26] Y.X. Duan, F.L. Meng, K.H. Liu, S.S. Yi, S.J. Li, J.M. Yan, et al., Adv. Mater. 30 (2018) 1706194.
[27] Y. Xiong, B. Wei, M. Wu, B. Hu, F. Zhu, J. Hao, et al., J. CO_2 Util. 51 (2021) 101621.
[28] C. Chen, X. Yan, Y. Wu, X. Zhang, S. Liu, F. Zhang, et al., Nat. Commun. 14 (2023) 1092.
[29] A. Muthuperiyanayagam, D. Di Tommaso, Electrochim. Acta 507 (2024) 145188.
[30] K.V. Tian, G.A. Chass, D.D. Tommaso, Phys. Chem. Chem. Phys. 18 (2015) 837–845.
[31] A. Tilocca, Phys. Rev. B 76 (2007) 224202.
[32] R. Jinnouchi, S. Minami, ACS Nano 19 (2025) 22600–22644.
[33] S.D.W. Wendji, R. Piotrowski, A. Familiari, C. Massobrio, M. Boero, C. Tugène, et al., Chem. Commun. (2025). https://pubs.rsc.org/en/content/articlelanding/2025/cc/d5cc00443h.
[34] H. Song, Y.C. Tan, B. Kim, S. Ringe, J. Oh, ACS Appl. Mater. Interfaces 13 (2021) 55272–55280.
[35] V. Romanovski, N. Sdobnyakov, S. Roslyakov, A. Kolosov, K. Podbolotov, K. Savina, et al., Inorg. Chem. 63 (2024) 24844–24854.
[36] M. Li, Y. Cao, J. Dang, S. Cui, W. Cui, Z. Li, et al., Appl. Surf. Sci. 684 (2025) 161864.
[37] E. Pedretti, P. Restuccia, M.C. Righi, Comput. Phys. Commun. 291 (2023) 108827.
[38] TriboTeam, Xsorb, GitLab (2024). https://gitlab.com/triboteam/xsorbed.
[39] B. Chang, H. Pang, F. Raziq, S. Wang, K.W. Huang, J. Ye, et al., Energy Environ. Sci. 16 (2023) 4714–4758.
[40] Z. Yan, W. Liu, X. Liu, Z. Shen, X. Li, D. Cao, Adv. Mater. Interfaces 10 (2023) 2300186.
[41] Q. Zhu, X. Sun, D. Yang, J. Ma, X. Kang, L. Zheng, et al., Nat. Commun. 10 (2019) 3851.
[42] C. Zhan, F. Dattila, C. Rettenmaier, A. Herzog, M. Herran, T. Wagner, et al., Nat. Energy 9 (2024) 1485–1496.
[43] X. Wang, Z. Wang, T.T. Zhuang, C.T. Dinh, J. Li, D.H. Nam, et al., Nat. Commun. 10 (2019) 5186.
[44] R. Jinnouchi, F. Karsai, G. Kresse, Phys. Rev. B 100 (2019) 014105.
[45] G. Kresse, J. Furthmüller, Comput. Mater. Sci 6 (1996) 15–50.
[46] G. Kresse, D. Joubert, Phys. Rev. B 59 (1999) 1758–1775.
[47] J.P. Perdew, K. Burke, M. Ernzerhof, Phys. Rev. Lett. 77 (1996) 3865–3868.
[48] S. Grimme, J. Antony, S. Ehrlich, H. Krieg, J. Chem. Phys. 132 (2010) 154104.
[49] W. Tang, E. Sanville, G. Henkelman, J. Phys. Condens. Matter 21 (2009) 084204.
[50] G. Henkelman, A. Arnaldsson, H. Jónsson, Comput. Mater. Sci 36 (2006) 354–360.
[51] E. Sanville, S.D. Kenny, R. Smith, G. Henkelman, J. Comput. Chem. 28 (2007) 899–908.
[52] X. Li, W. Paier, J. Paier, Front. Chem. 8 (2020) 601029.
[53] P. Liu, C. Verdi, F. Karsai, G. Kresse, Phys. Rev. Mater. 5 (2021) 053804.
[54] V.L. Deringer, M.A. Caro, G. Csányi, Adv. Mater. 31 (2019) 1902765.
[55] K.V. Tian, M.Z. Mahmoud, P. Cozza, S. Licoccia, D.C. Fang, D. Di Tommaso, et al., J. Non-Cryst. Solids 451 (2016) 138–145.
[56] D. Di Tommaso, R.I. Ainsworth, E. Tang, N.H. de Leeuw, J. Mater. Chem. B 1 (2013) 5054.
[57] K.V. Tian, G.A. Chass, D.D. Tommaso, Phys. Chem. Chem. Phys. 18 (2016) 837–845.
[58] TriboTeam, Workflow, GitLab (2024). https://gitlab.com/triboteam/xsorbed/-/wikis/Workflow.
[59] H. Pan, A.M. Ganose, M. Horton, M. Aykol, K.A. Persson, N.E.R. Zimmermann, et al., Inorg. Chem. 60 (2021) 1590–1603.
[60] K. Mathew, R. Sundararaman, K. Letchworth-Weaver, T.A. Arias, R.G. Hennig, J. Chem. Phys. 140 (2014) 084106.
[61] Q. Zhang, A. Asthagiri, Catal. Today 323 (2019) 35–43.
[62] J.K. Nørskov, J. Rossmeisl, A. Logadottir, L. Lindqvist, J.R. Kitchin, T. Bligaard, et al., J. Phys. Chem. B 108 (2004) 17886–17892.
[63] J.H. Liu, L.M. Yang, E. Ganz, J. Mater. Chem. A 7 (2019) (1952) 11944.
[64] A. Tilocca, A.N. Cormack, ACS Appl. Mater. Interfaces 1 (2009) 1324–1333.
[65] J. Hu, A. Al-Salihy, B. Zhang, S. Li, P. Xu, Int. J. Mol. Sci. 23 (2022) 15405.
[66] L. Ou, W. Long, J. Huang, Y. Chen, J. Jin, RSC Adv. 7 (2017) (1950) 11938.
[67] F. Tang, L. Wang, M. Dessie Walle, A. Mustapha, Y.N. Liu, J. Catal. 383 (2020) 172–180.
[68] R. Yun, B. Zhang, C. Shi, R. Xu, T. Suo, Inorg. Chem. 62 (2023) 15790–15796.
[69] X. Zhang, C. Liu, Y. Zhao, L. Li, Y. Chen, F. Raziq, et al., Appl. Catal. B 291 (2021) 120030.
[70] N. Jeyachandran, W. Yuan, X. Li, A. Muthuperiyanayagam, S. Gardoni, J. Feng, et al., Appl. Mater. Today 41 (2024) 102466.